Research Article | Open Access

Soft Science

Kim *et al. Soft Sci.* **2026**, *6*, 47 **DOI:**10.20517/ss.2026.07

Laser-triggerable elastomeric composites for soft electronics and robotics

Kyung-Sub Kim[1,#], Min-Ha Oh[2,3,#], Jieun Han[3], Yoon-Nam Kim[3], Jae-Young Bae[1], Yong-Wu Kim[3], Yong-Joong Shin[3], Jae-Hwan Lee[4], Sung-Woo Kim[3], Edyta Wyszkowska[5], Sang Yup Kim[6], Seung-Kyun Kang[1,3,4,7,*]

Keywords:
Laser-triggered decomposition, on-demand degradation, transient silicone elastomers, transient electronics, transient soft actuators, shape-shifting soft robots

Citation: Kim, K. S.; Oh, M. H.; Han, J.; Kim, Y. N.; Bae, J. Y.; Kim, Y. W.; Shin, Y. J.; Lee, J. H.; Kim, S. W.; Wyszkowska, E.; Kim, S. Y.; Kang, S. K. Laser-triggerable elastomeric composites for soft electronics and robotics. *Soft Sci.* **2026**, *6*, 47. https://dx.doi.org/10.20517/ss.2026.07

Received: 14 Jan 2026 **First Decision:** 19 Mar 2026 **Revised:** 30 Apr 2026 **Accepted:** 7 May 2026 **Published:** 12 Jun 2026

Academic Editor: YongAn Huang
Copy Editor: Shu-Yuan Duan
Production Editor: Shu-Yuan Duan

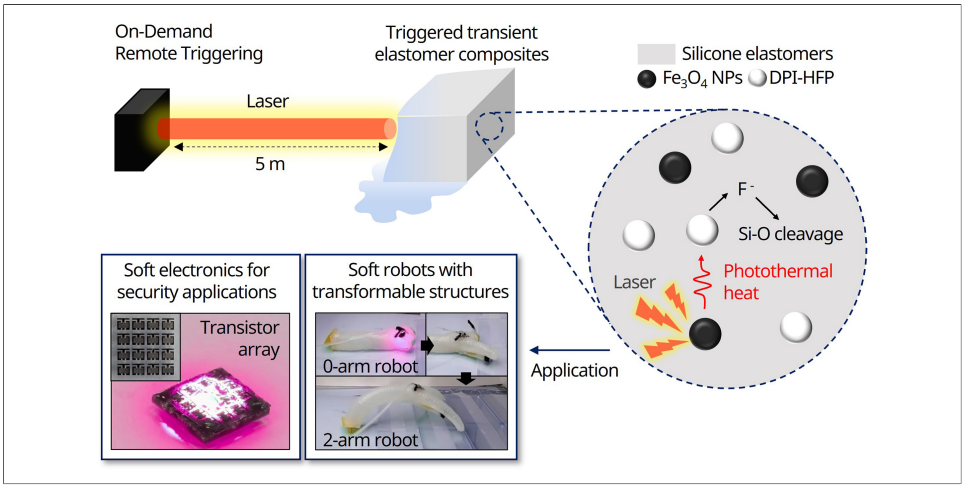

Abstract

Remotely triggerable transient materials can couple on-demand functional reconfiguration with clean end-of-life control in soft systems. Here, we present a laser-addressable silicone elastomer composite that undergoes rapid thermochemical liquefaction under femtosecond laser pulses. The composite integrates Fe_3O_4 nanoparticles (Fe_3O_4 NPs) as photothermal transducers and diphenyliodonium hexafluorophosphate (DPI-HFP) powders as thermally activated fluoride generators, which catalyze Si-O bond cleavage. Localized photothermal heating initiates decomposition at moderate fluence and enables device-scale erasure under significantly lower energy input than direct laser ablation of pristine Ecoflex. Systematic studies elucidate how photothermal filler content and thermal conductivity determine triggering thresholds and govern decomposition kinetics. Before triggering, the material retains high elasticity and mechanical robustness, enabling its use as a substrate for stretchable electronics and as a strain-limiting layer for transformable

[1]Research Institute of Advanced Materials (RIAM), Seoul National University, Seoul 08826, Republic of Korea.
[2]Samsung Electronics Co. Ltd., Semiconductor R&D Center, Hwaseong-si 18448, Republic of Korea.
[3]Department of Materials Science and Engineering, Seoul National University, Seoul 08826, Republic of Korea.
[4]Nano Systems Institute SOFT Foundry, Seoul National University, Seoul 08826, Republic of Korea.
[5]National Centre for Nuclear Research, NOMATEN CoE MAB+, Otwock 05-400, Poland.
[6]Department of Mechanical Engineering, Sogang University, Seoul 04107, Republic of Korea.
[7]Interdisciplinary Program of Bioengineering, Seoul National University, Seoul 08826, Republic of Korea.
[#]These authors contributed equally to this work.

[*]**Correspondence to:** Prof. Seung-Kyun Kang, Department of Materials Science and Engineering, Seoul National University, Seoul 08826, Republic of Korea. E-mail: kskg7227@snu.ac.kr

soft actuators. Proof-of-concept devices demonstrate spatially selective erasure of electronic components and remote reprogramming of actuator kinematics without contact or bulk heating. This elastomeric transient platform bridges mechanical compliance with stand-off and programmable termination, providing a route to spatiotemporally resolved state control in soft electronics and robotics.

INTRODUCTION

Driven by the growing demand for shape-adaptive systems, stimuli-responsive materials that can actively change their shape, function, or properties have attracted significant attention in soft electronics and robotics[1-4]. These materials can be engineered to respond to various stimuli including light[5-8], heat[4,7-11], moisture[12], ultrasound[13], and electrical signals[11,14-16], and employ mechanisms such as controlled degradation[6-8,12,13], structural morphing[5,14-16], and phase transitions[9-11,17] to achieve functional transformation under specific environmental conditions. Examples include soft robotic actuators that alter their geometry during operation to enhance mobility and environmental adaptability[5,11,14-16,18], and soft electronic systems in which transient devices disintegrate under programmed conditions to improve environmental sustainability and data security[6,7,9,10,12]. Incorporating remote control into such systems further expands their utility in environments with limited accessibility, offering spatiotemporal programmability and increased design flexibility[5-8].

Triggered transient systems are particularly attractive for applications that require on-demand transformation or termination of function. Examples include soft robotic actuators that can alter motion patterns mid-operation[7], and transient electronic circuits that shift or turn off functionality under specific conditions[13]. Despite their potential, current systems face key challenges in remote control range, mechanical robustness, and operational stability. For example, metastable cyclic poly(phthalaldehyde) (cPPA) degrades at elevated temperatures but requires proximity to a heat source, limiting its applicability for stand-off control[6]. cPPA-based composites responsive to light partially address this limitation[6], yet they lack stretchability and durability and are prone to unintentional degradation under ambient conditions. Other triggered systems, including moisture-responsive polyanhydride[12] and ultrasound-responsive poly(3-hydroxybutyrate-co-3-hydroxyvalerate) (PHBV)[13], have also been explored, but achieving long-range triggering together with high mechanical performance and stability remains a challenge.

Silicone elastomer-based transient systems have recently emerged as promising candidates due to their inherent stretchability, flexibility, and durability[7,8]. For instance, hyperelastic silicone elastomer composites containing the photo-fluoride generator, which decompose upon ultraviolet (UV) and heat exposure, have been reported for use in pneumatic soft robots[7]. However, the low penetration depth of UV light hampers efficient triggering of bulk soft devices and requires substantial energy input. Silicone composites incorporating fluoride-ion-amplifying molecules significantly reduce the total energy required for decomposition[8], but remote triggering remains challenging due to the requirement for simultaneous exposure to UV and heat. While lasers offer an attractive means for remote energy delivery, conventional laser-based elastomer transformation relies on direct ablation, which requires high energy input and results in low efficiency[19]. These limitations highlight the need for flexible, durable, and energy-efficient shape-adaptive materials that can be remotely triggered from a distance. Such materials will be critical for advancing environmentally adaptive transient platforms in soft electronics and robotics.

Here, we present an elastomeric composite that undergoes rapid thermochemical decomposition into a liquid phase upon femtosecond laser application from distances exceeding 5 m. The system incorporates photothermal Fe_3O_4 nanoparticles (Fe_3O_4 NPs) and the thermally activated fluoride generator diphenyliodonium hexafluorophosphate (DPI-HFP), which together lower the activation energy required for

Si-O bond cleavage. This approach achieves complete decomposition under significantly lower energy input than direct laser ablation of pristine Ecoflex. We further examine how the thermal conductivity of photothermal fillers influences decomposition efficiency and analyze decomposition kinetics as functions of filler content and laser power. The optimized composite retains high elasticity and mechanical robustness, enabling its use as a substrate for rapidly decomposable soft electronic devices and as a strain-limiting element in transformable soft actuators. These demonstrations establish remotely triggerable elastomeric composites as a platform for spatiotemporally programmable soft systems.

EXPERIMENTAL

Preparation of DPI-HFP/photothermal particle/silicone composite

To prepare the DPI-HFP/Fe_3O_4 NPs/Ecoflex 00-30 composite, the required amounts of diphenyl iodonium hexafluorophosphate (DPI-HFP; TCI, Japan) and Fe_3O_4 NPs (diameter 50-100 nm; Sigma-Aldrich) were added to the Ecoflex 00-30 pre-polymer (A:B = 1:1 by mass; Smooth-On, USA). The mixture was then mechanically blended using a centrifugal mixer (ARE-310, Thinky, Japan). After mixing, it was degassed in a vacuum desiccator for 5 min to remove air bubbles, poured onto a glass substrate, and cured at room temperature for 4 h. A similar procedure was used to prepare the DPI-HFP/Fe_3O_4 NPs/Sylgard-184 composite, using Sylgard-184 (Dow Corning, USA) with a pre-polymer mixing ratio of 20:1 and a curing time of 24 h. For the DPI-HFP/carbon black/Ecoflex 00-30 composite, the same method was followed, except that Fe_3O_4 NPs were replaced with carbon black (diameter < 100 nm; Sigma-Aldrich). To achieve high decomposition efficiency without compromising the mechanical properties of the composites, the concentration of DPI-HFP was fixed at 10 wt.% in all experiments[7]. For the decomposition kinetics analysis, samples were prepared with varying Fe_3O_4 nanoparticle contents of 0.10, 0.25, 0.50, 0.75, and 1.00 wt.%. For all experiments other than the decomposition kinetics analysis, samples containing 1.00 wt.% Fe_3O_4 nanoparticles, which exhibited the highest decomposition efficiency, were used.

Triggered decomposition experiments

DPI-HFP/photothermal particle/silicone composites were decomposed via laser triggering using a femtosecond pulsed laser (spot size = 8 mm (diameter), λ = 800 nm, pulse width = ~ 100 fs, Mai-Tai-HP, Spectra-Physics, USA) positioned 5 meters away. Devices fabricated from these composites were also tested under the same conditions. The process was performed for the necessary durations at a power level below 0.5 W, without applying any additional UV or thermal treatment. For comparison, the UV- and heat-triggered decomposition of the DPI-HFP/Fe_3O_4 NPs/Ecoflex 00-30 composite was conducted by exposing it to a 30 W UV lamp (λ = 365 nm; VL-215L, Viber Lourmat, France) for 30 min and by heating it on a 120 °C hot plate (MSH-20D, DAIHAN-Science, Korea) for the required durations.

Decomposition analysis of DPI-HFP/Fe_3O_4 NPs/Ecoflex 00-30 composite

Thermogravimetric analysis (TGA) and differential scanning calorimetry (DSC) of the DPI-HFP/Ecoflex 00-30 composites were performed under a nitrogen atmosphere using a thermal analysis system (TGA/DSC 3+, Mettler Toledo, Switzerland). The thermal distribution images of the composites were captured using a thermal camera (FLIR A6700 MWIR, Teledyne FLIR, USA) during laser-triggered decomposition. To analyze the decomposition chemistry, IR spectroscopy was performed using a Nicolet iS50 Fourier-transform infrared (FT-IR) spectrophotometer (Thermo Fisher Scientific, USA). Solid-state ^{29}Si- and ^{1}H-nuclear magnetic resonance (NMR) data were recorded on a 500 MHz Avance III system (Bruker, Germany), using pulse sequences of 42 and 60, spinning rates of 5 and 10 kHz, recycle delays of 60 and 3 s, and 300 and 32 scans for ^{29}Si and ^{1}H measurements, respectively.

Measurement of mechanical properties of DPI-HFP/Fe_3O_4 NPs/Ecoflex 00-30 composites

Tensile tests were performed on DPI-HFP (10 wt.%)/Fe_3O_4 NPs (1.00 wt.%)/Ecoflex 00-30 specimens prepared in accordance with ISO 527-2:2012 (Type 5A, gauge length 25 mm, gauge width 4 mm, overall length 75 mm, and thickness 2 mm). Mechanical properties were measured using a tensile testing machine (68TM-5, Instron 3343, USA) equipped with a 50 N load cell, applying a strain rate of 50% per min.

Fabrication of stretchable devices with DPI-HFP/Fe_3O_4 NPs/Ecoflex 00-30 substrate

First, a polybutylene adipate terephthalate (PBAT) film (~ 30 μm thick) was formed by spin-coating (1,000 rpm, 30 s) and solvent evaporation of a solution containing PBAT (3 g, SEnPol, Korea) and chloroform (10 mL, DAEJUNG, Korea) onto a slide glass that had been surface-treated with a self-assembled monolayer (SAM). The SAM treatment was performed by immersing the slide glass in a solution of octadecyltrimethoxysilane (100 μL, Sigma-Aldrich) in hexane (60 mL, DAEJUNG, Korea) for 1.5 h. Next, an adhesion layer of Cr (~ 15 nm) and a conductive Au layer (~ 75 nm) were deposited onto the PBAT film using sputtering (J Vacuum Technology, Korea). The resulting Au/Cr/PBAT film on the slide glass was then patterned into serpentine-shaped interconnecting wires with light-emitting diode (LED) pads, an interdigitated capacitive strain sensor, and resistive temperature sensors by laser cutting (3 W, 50 kHz, 50 mm/s) (MD-U1000C, Keyence, Japan). Unwanted areas were removed, and the LED chips were electrically connected to the LED pads using silver epoxy (8331S, MG Chemicals, Canada). Copper tape was also attached to the pads located at the measurement terminals of all devices. Finally, uncured DPI-HFP/Fe_3O_4 NPs/Ecoflex 00-30 was poured over the patterned structure to the desired thickness and cured; after curing, the device was peeled off from the glass substrate, completing the fabrication process.

Fabrication of transient n-channel metal-oxide-semiconductor field-effect transistor arrays on DPI-HFP/Fe_3O_4 NPs/Ecoflex 00-30

The fabrication of an n-channel metal-oxide-semiconductor field-effect transistor (MOSFET) (NMOS) began with the deposition of a silicon dioxide (SiO_2, ~ 600 nm) layer by plasma-enhanced chemical vapor deposition (PECVD) on a silicon-on-insulator (SOI, top silicon ~ 400 nm, SOITEC) substrate, serving as a doping mask. The doping regions were defined by patterning the mask with buffered oxide etchant (6:1, Transene), followed by thermal diffusion of spin-on dopant (P509, Filmtronics) at 1,050 °C for 5 min. To release the doped top silicon, 5 μm × 5 μm holes were patterned in the top silicon layer, and the buried oxide (BOX, ~ 1 μm) was etched in 49% hydrofluoric acid (Transene) for 30 min. The released phosphorus-doped silicon nanomembrane was subsequently transferred onto a polyimide (PI, ~ 1 μm) spin-coated on a silicon wafer. The channel arrays were isolated by reactive ion etching (RIE, J Vacuum Technology). A 100 nm-thick SiO_2 was then deposited by PECVD and patterned using buffered oxide etchant (6:1, Transene) to define the gate dielectric. A 400 nm-thick Mo layer was deposited via sputtering, and gate/source/drain electrodes were defined by a lift-off process (nLOF2070, MicroChemicals). The NMOS arrays on a polyimide (PI) substrate were picked off from the silicon wafer using a PDMS stamp, and RIE removed the underlying PI layer. The NMOS arrays were integrated onto a PBAT substrate through heat sealing at 120 °C. The NMOS/PBAT devices were patterned into square geometries using UV laser processing (MD-U1000C, Keyence). Finally, uncured DPI-HFP/Fe_3O_4 NPs/Ecoflex 00-30 was poured over the NMOS/PBAT and then cured to complete the device.

Evaluation of the various electronics

Calibration of the strain sensor was performed by recording capacitance changes with a custom-built circuit while the device was subjected to cyclic stretching and contraction at a rate of 8% per s. The inherent ~ 25 pF stray capacitance of the Arduino Uno enabled capacitance readings from the sensors wired to pins A0 and A2. The temperature sensor array was characterized by measuring its resistance using a multi-channel digital multimeter (PXIe-4081, National Instruments, USA). The electrical characteristics, including I-V and

transfer curves, of the n-channel MOSFET were measured using a semiconductor analyzer (4200A-SCS, Keithley, USA).

Fabrication of transformable soft robots

First, uncured Ecoflex 00-30 was applied to a 3D-printed mold and combined with other components to fabricate zigzag-shaped actuators. DPI-HFP/Fe_3O_4 NPs/Sylgard-184 strain limiters were also produced in 3D-printed molds. An uncured DPI-HFP/ Fe_3O_4 NPs/Sylgard-184 mixture was applied between the zigzag actuators and the strain limiters, followed by curing at 60 °C for 1 h. The cured material then functioned as a strain-limiting layer. The legless soft crawler was fabricated by rolling a sheet of Ecoflex 00-30 (~ 1.5 mm thick) embedded with evenly spaced high-strength fibers into a hollow cylindrical bending body. The edges were sealed using high-modulus Dragon Skin 20 (Smooth-On, USA) to maintain the shape and enhance stiffness. To reduce ground friction, PI tape was attached to the front strain limiter area. The bending legs were constructed similarly by rolling Ecoflex 00-30 sheets embedded with fibers and sealing with Dragon Skin 20. Strain limiters, designed to prevent leg extension during pneumatic actuation initially, were fabricated from flat Ecoflex 00-30 sheets and bonded to the openings of the bending body using a triggerable adhesive composed of DPI-HFP/Fe_3O_4 NPs/Ecoflex 00-30.

RESULTS AND DISCUSSION

Remote laser-triggered decomposition mechanism of DPI-HFP/Fe_3O_4 NPs/ecoflex composites

Figure 1A illustrates the remote triggering system designed to induce thermochemical decomposition of the Ecoflex 00-30 matrix by laser. The system incorporates Fe_3O_4 nanoparticles (NPs) and DPI-HFP powder into the composite. When a femtosecond pulsed laser (λ = 800 nm, pulse width ~ 100 fs) is applied, heat generated from the photothermal Fe_3O_4 NPs (50-100 nm) activates DPI-HFP to release fluoride ions[8,20,21]. These fluoride ions initiate a cascade of reactions that cleave Si-O bonds, leading to the decomposition of the silicone matrix[22,23]. The heat generated by the photothermal effect of Fe_3O_4 NPs serves as the primary thermal input that facilitates fluoride-induced bond cleavage, while the exothermic processes associated with DPI-HFP and subsequent reactions may provide additional thermal assistance[7,8,24]. After laser activation, the final products consist of a liquid residue derived from the silicone and a small amount of residual Fe_3O_4 NPs.

Figure 1B shows laser-triggered decomposition in a physical sample. A composite block composed of DPI-HFP (10 wt.%), Fe_3O_4 NPs (1.00 wt.%), and Ecoflex 00-30 (5 mm × 5 mm × 5 mm) was exposed to a laser beam (power = 0.25 W) emitted from a source placed 5 meters away. Decomposition initiates at the top surface, where the laser is first applied, and progresses downward. After 15 min, nearly the entire silicone matrix is converted into a liquid phase, while Fe_3O_4 NPs remain as undissolved residues [Supplementary Video 1]. As shown in Figure 1B, the final decomposition product forms a liquid residue that can be easily removed with a swab. Complete decomposition of the composite is achieved within approximately 10 min at 0.5 W or 20 min at 0.25 W of laser power. The energy required to degrade 1 cm^3 of the composite is estimated to be 1.19 kJ (fluence: 1.243×10^{-8} J·cm^{-2}·$pulse^{-1}$), which is substantially lower than the 21.97 kJ (fluence: 132.6 J·cm^{-2}·$pulse^{-1}$) required for ablating pristine Ecoflex [see Supplementary Text][19]. This comparison illustrates the difference in energy scale between thermochemical decomposition and direct laser ablation, as the two processes involve distinct mechanisms and irradiation conditions. This reduced energy demand is attributed to the thermochemical synergy between Fe_3O_4 NPs and DPI-HFP, which lowers the overall activation energy of the degradation process[7,8,24].

To better understand the thermally induced decomposition mechanism underlying our laser-triggered system, we investigated the thermal reactivity of DPI-HFP in the absence of UV exposure. Although DPI-HFP is typically known as a photo-fluoride generator, it also functions effectively as a thermal fluoride generator. Prior work has shown that DPI-HFP begins releasing fluoride ions at temperatures exceeding

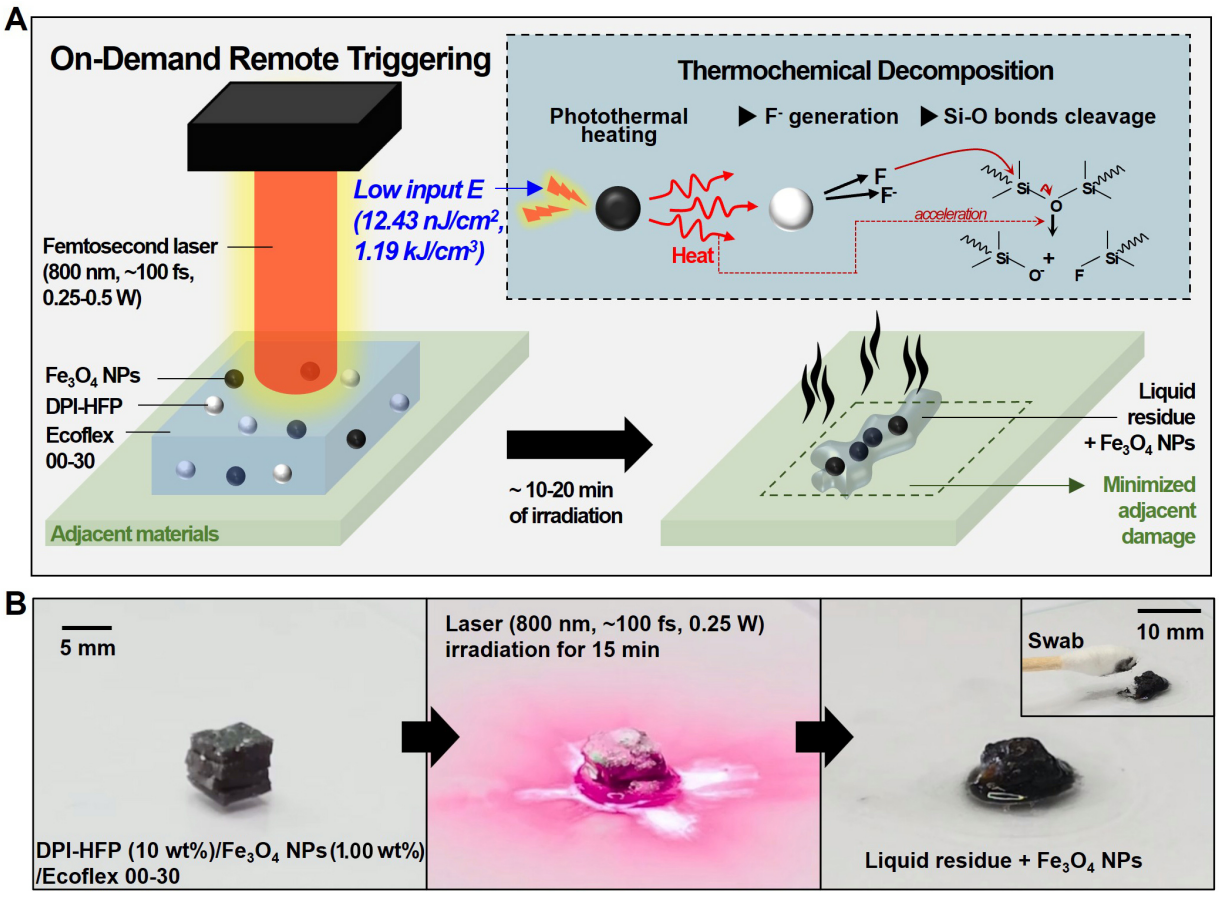

Figure 1. Mechanism of laser-triggered remote decomposition of DPI-HFP/Fe_3O_4 NPs/Ecoflex 00-30 composites. (A) A schematic illustrating the degradation mechanism of DPI-HFP/Fe_3O_4 NPs/silicone composites under femtosecond pulsed laser irradiation. The DPI-HFP/Fe_3O_4 NPs/silicone composites (left) produce fluoride ions via the photothermal effect of Fe_3O_4 NPs (middle), leading to their decomposition into liquid residue and Fe_3O_4 NPs (right). (B) Serial images showing the DPI-HFP (10 wt.%)/Fe_3O_4 NPs (1.00 wt.%)/Ecoflex 00-30 composite before (left), during (middle), and after (right) 800 nm laser irradiation (spot size = 8 mm (diameter), pulse width = ~ 100 fs, power = 0.25 W) for 15 min, without prior UV or heat treatment. NP: Nanoparticle; DPI-HFP: diphenyliodonium hexafluorophosphate; UV: ultraviolet.

239.2 °C without the need for UV activation[8], following a mechanism similar to that observed under UV irradiation [Supplementary Figure 1A]. Supplementary Figure 1B presents a series of images showing the complete decomposition of a DPI-HFP (10 wt.%)/Ecoflex composite without any UV exposure after heating at 240 °C for 30 min. To further validate this thermally induced decomposition pathway, we performed thermal analysis on neat Ecoflex and DPI-HFP/Ecoflex composites without Fe_3O_4 NPs. Thermogravimetric analysis (TGA) and differential scanning calorimetry (DSC) were conducted under nitrogen [Supplementary Figure 1C and D]. The decomposition onset temperatures of neat Ecoflex, the UV-unexposed composite, and the UV-exposed composite were approximately 400 °C, 240 °C, and 235 °C, respectively [Supplementary Figure 1C]. Although the UV-unexposed composite required slightly higher temperatures than the UV-pretreated sample, its onset temperature was significantly lower than that of neat Ecoflex, confirming the effectiveness of thermal activation. In DSC analysis, the composite without UV exposure showed enhanced exothermic energy above ~ 350 °C, while the UV-exposed composite exhibited increased heat release across the entire temperature range [Supplementary Figure 1D]. This higher exothermicity is attributed to the dual thermal processes involving fluoride ion generation from DPI-HFP and subsequent Si-O bond cleavage.

Effects of the thermal conductivity of photothermal fillers on the decomposition efficiency of the composites

The thermal conductivity of the photothermal filler is a key factor in determining the decomposition efficiency of bulk composites, as it governs heat transfer in systems with limited laser light penetration[25-27]. Various photothermal materials, such as graphene, carbon nanotubes, gold, and silver, can be incorporated into this system[28-30]; in this study, carbon black was selected as a representative comparator to Fe_3O_4 NPs.

Figure 2A-D presents morphological and thermographic images of DPI-HFP (10 wt.%)/Ecoflex composites containing 1.00 wt.% of either Fe_3O_4 NPs or carbon black, both before and after laser triggering (λ = 800 nm, pulse width ~ 100 fs, laser power = 0.25 W). The laser was positioned 5 m away and targeted the top surface of 2 mm-thick composite sheets over an 8 mm-diameter circular area. After 5 min of laser application, the Fe_3O_4 NPs composite decomposed to a depth of ~ 1.7 mm, leaving an oily residue [Figure 2A], and the temperature at the triggered region rose sharply from 24.0 °C to 285.4 °C within 1 min [Figure 2B, Supplementary Video 2]. In contrast, the carbon black composite decomposed to a depth of ~ 0.9 mm [Figure 2C], with the central temperature increasing from 23.1 °C to 323.1 °C over the same period [Figure 2D, Supplementary Video 3]. Despite having a slightly lower specific heat capacity than carbon black[31,32], the Fe_3O_4 NPs composite initially exhibited a lower surface temperature. This is likely due to localized heat accumulation at the carbon black composite surface, caused by its higher absorption coefficient[20,33] and lower thermal conductivity[31,32,34,35] compared to Fe_3O_4 NPs. After 5 min of continuous laser application, however, the surface temperature of the Fe_3O_4 NPs composite reached 406.6 °C, surpassing the 324.6 °C of the carbon black composite [Figure 2E]. This higher temperature led to greater decomposition depth in the Fe_3O_4 NPs composite. The improved decomposition efficiency is primarily attributed to the higher thermal conductivity of Fe_3O_4 NPs[31,32,34,35]. At the same time, differences in filler dispersion and interfacial characteristics may also have contributed, with thermal transport playing a dominant role in promoting more uniform heat transfer throughout the composite[33-35]. Side-view thermographic images of 8 mm-thick samples further confirm that the Fe_3O_4 NPs composite transfers heat more effectively into the interior than the carbon black composite [Figure 2F and G].

When the same laser conditions were applied to a DPI-HFP (10 wt.%)/Ecoflex composite without any photothermal filler, no decomposition occurred, and the temperature change was minimal [Supplementary Figure 2A-C and Supplementary Video 4]. Similarly, the Fe_3O_4 NPs (1.00 wt.%)/Ecoflex composite without DPI-HFP showed no visible damage, although the surface temperature reached 244.7 °C within 1 min due to the photothermal effect of Fe_3O_4 NPs [Supplementary Figure 2C-E, Supplementary Video 5]. This temperature remained around 245 °C even after 5 min of continued laser application, which is substantially lower than the 406.6 °C reached by the DPI-HFP/Fe_3O_4 NPs/Ecoflex composite [Figure 2E]. These results indicate that DPI-HFP not only supplies fluoride ions for initiating Si-O bond cleavage, but also contributes to significant heat generation through exothermic reactions during both fluoride generation and bond cleavage. At the same time, the breakdown of the polymer network during decomposition may alter or reduce heat transfer pathways, leading to localized heat accumulation and the formation of hot spots. In addition, the liquid-like state formed after decomposition retains relatively high viscosity, which can limit convective heat dissipation and further enhance heat accumulation. These factors, acting in combination, are likely to have reduced the energy required for laser-induced decomposition compared to conventional physical ablation.

Decomposition chemistry and kinetics of DPI-HFP/Fe_3O_4 NPs/silicone elastomer composites

Figure 3A and B and Supplementary Figure 3 present spectroscopy data obtained during the remote triggering of the DPI-HFP/Fe_3O_4 NPs (1.00 wt.%)/Ecoflex 00-30 composite using the laser (laser power = 0.25 W, distance = 5 meters) for elucidating its decomposition mechanism. Figure 3A displays FT-IR spectra,

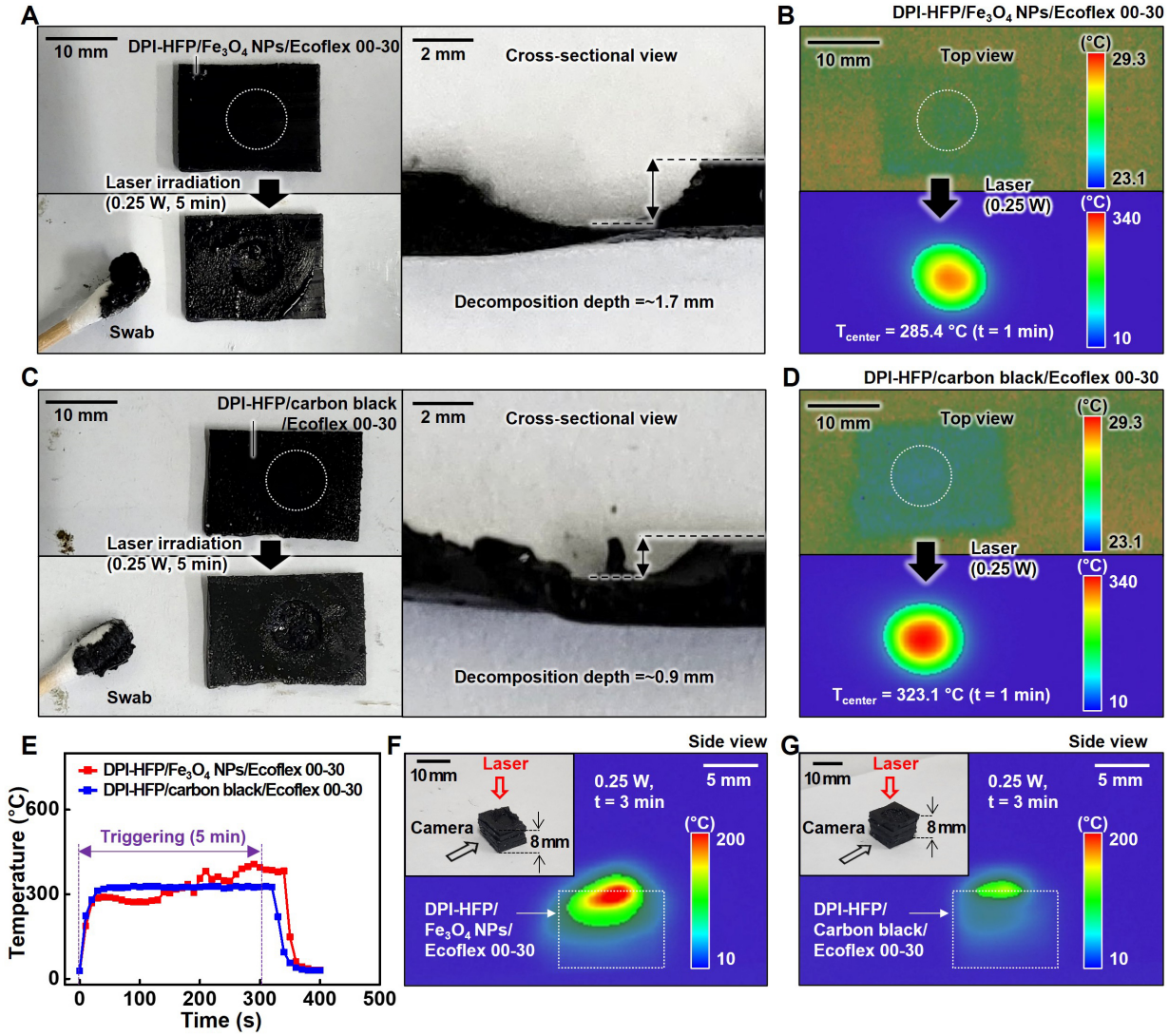

Figure 2. Comparison of decomposition efficiency of Fe_3O_4 NPs-based and carbon black-based silicone composites. (A) Morphological images of DPI-HFP/Fe_3O_4 NPs (1.00 wt.%)/Ecoflex 00-30 sheets before (top left) and after (bottom left, top view; right, cross-sectional view) laser exposure (5 min); (B) Thermographic images of DPI-HFP/Fe_3O_4 NPs/Ecoflex 00-30 sheets before (top) and after (bottom) laser exposure (1 min); (C) Morphological images of DPI-HFP/carbon black (1.00 wt.%)/Ecoflex 00-30 sheets before (top left) and after (bottom left, top view; right, cross-sectional view) laser exposure (5 min); (D) Thermographic images of DPI-HFP/carbon black/Ecoflex 00-30 sheets before (top) and after (bottom) laser exposure (1 min); (E) Temperature profile of the silicone composites during 5 minutes of laser triggering (DPI-HFP/Fe_3O_4 NPs/Ecoflex 00-30, red; DPI-HFP/carbon black/Ecoflex 00-30, blue). Side-view thermographic images of (F) DPI-HFP/Fe_3O_4 NPs/Ecoflex 00-30 and (G) DPI-HFP/carbon black/Ecoflex 00-30 taken 3 min after laser triggering. [Thickness of sheets: (A-D), 2 mm; (F and G) 8 mm; Laser condition: spot size = 8 mm (diameter), laser power = 0.25 W, λ = 800 nm, pulse width = ~ 100 fs]. NP: Nanoparticle; DPI-HFP: diphenyliodonium hexafluorophosphate.

showing reductions in the Si-O-Si bond peak at 1,013 cm^{-1} and the Si-CH_3 bond peak at 792 cm^{-1} following laser exposure. This confirms that the Si-O bonds are cleaved by fluoride ions and the Si-CH_3 bonds are cleaved by the Pt catalyst [Supplementary Figure 4][7,36,37]. Supplementary Figure 3 shows the ^{29}Si-NMR spectra, which reveal a decrease in the in-chain Si peak at -40 ppm, further supporting Si-O bond cleavage. Solid-state ^{1}H-NMR relaxometry in Figure 3B reveals an increase in the T_2 relaxation time of the composite after laser exposure, suggesting de-crosslinking and fragmentation of the organosilicon network[38]. Since Sylgard-184 elastomer has a chain-like structure similar to that of Ecoflex 00-30, previous studies have reported that the decomposition mechanism mediated by fluoride ions in DPI-HFP-containing composites is also applicable to Sylgard-184[7,8]. We also evaluated the decomposition kinetics of Sylgard-184-based composites.

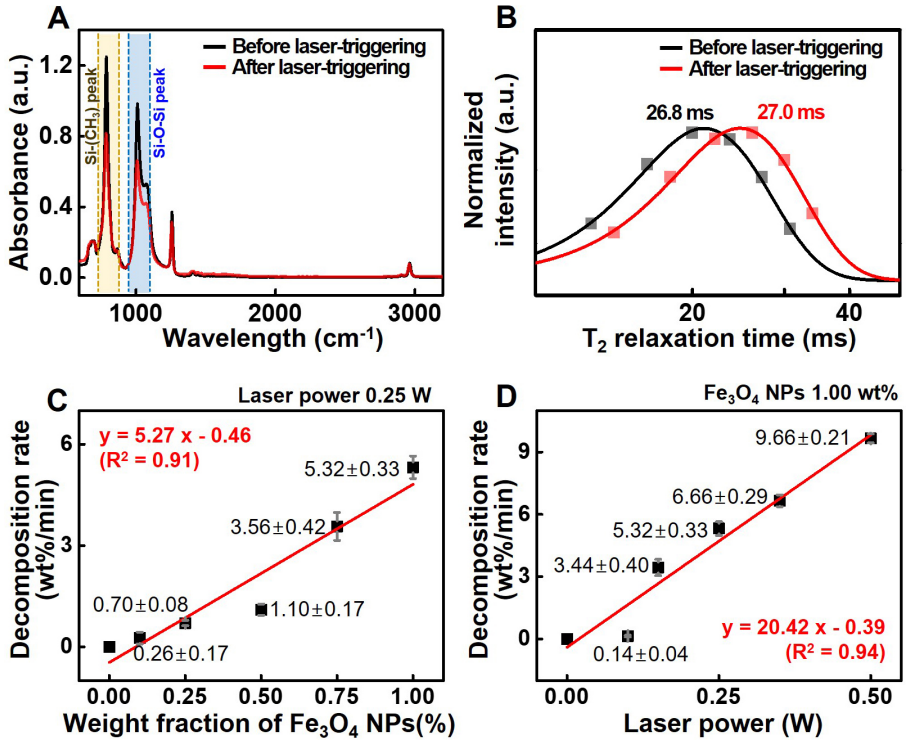

Figure 3. Laser-triggered decomposition chemistry and kinetics of DPI-HFP/Fe_3O_4 NPs/ Ecoflex 00-30 composites. (A) Infrared spectra of DPI-HFP/Fe_3O_4 NPs (1.00 wt.%)/Ecoflex 00-30, showing absorbance decrease in Si-CH_3 peak (792 cm^{-1}) and Si-O-Si peak (1,013 cm^{-1}) after laser-triggering (0.25 W, 20 min); (B) Solid-state ^{1}H-NMR T_2 distributions of the composite. T_2 relaxation time increased after laser-triggering (0.25 W, 20 min), indicating a decrease in the crosslinking density. Decomposition behaviors of the composite (C) for various Fe_3O_4 NPs concentrations (laser power = 0.25 W); and (D) at different laser powers (Fe_3O_4 NPs, 1.00 wt.%). The femtosecond pulsed laser (spot size = 8 mm (diameter), λ = 800 nm, pulse width = ~ 100 fs) was applied to the composites from a light source positioned 5 meters away in all cases. (C and D) Data are presented as mean ± SD of *n* = 3 independent measurements. NP: Nanoparticle; DPI-HFP: diphenyliodonium hexafluorophosphate; NMR: nuclear magnetic resonance; SD: standard deviation.

Figure 3C and D illustrate the linear dependence of decomposition kinetics of DPI-HFP/Fe_3O_4 NPs/Ecoflex composites on the concentration of Fe_3O_4 NPs and laser power. The decomposition rates were 0.00, 0.26, 0.70, 1.10, 3.56, and 5.32 wt.% min^{-1} corresponding to weight fractions of Fe_3O_4 NPs of 0.00, 0.10, 0.25, 0.50, 0.75, and 1.00 wt.%, respectively, under 0.25 W of laser exposure [Figure 3C, Supplementary Figure 5A]. Composites without Fe_3O_4 NPs did not absorb the pulsed laser. The increase in Fe_3O_4 NPs concentration indicates a greater number of photothermal heating sites, which in turn accelerates the decomposition rate. For the composite with 1.00 wt.% of Fe_3O_4 NPs, the decomposition rates were recorded as 0.14, 3.44, 5.32, 6.66, and 9.66 wt.% min^{-1} at laser power levels of 0.10, 0.15, 0.25, 0.35, and 0.50 W, respectively [Figure 3D, Supplementary Figure 5B]. These trends followed linear relationships:

$r = -0.46 + 5.27f$ (Fe_3O_4 NPs weight fraction),
$r = -0.39 + 20.42p$ (laser power),

where r, f, and p denote the decomposition rate, filler weight fraction, and laser power, respectively. A similar linear trend was observed for DPI-HFP/Fe_3O_4 NPs/Sylgard-184 composites, with relationships [Supplementary Figure 5C-F]:

$r = 0.45 + 3.06f$,
$r = -1.16 + 20.42p$.

Due to its higher crosslinking density, Sylgard-184 composites exhibited lower slope values than those with Ecoflex[7]. The decomposition rates were calculated as the weight loss per unit time, and in all processes, the weight of the remaining solid composite was measured after gently washing the liquid residue with isopropyl alcohol.

The decomposition efficiency is expected to be influenced by laser parameters such as wavelength, which determines the temperature distribution and photothermal efficiency[39], pulse frequency, which governs thermal accumulation or plasma shielding effects[40], and laser spot size, which controls the energy density. In addition, the decomposition efficiency is also affected by the temperature and humidity surrounding the composite. The decomposition kinetics under varying laser parameters and environmental conditions are discussed in detail in the Supplementary Text and Supplementary Figure 6.

We further compared the decomposition performance of the laser triggering method with that of conventional UV/heat activation. Supplementary Figure 7A and B compare the decomposition rates of the DPI-HFP/Fe_3O_4 NPs/silicone composites under UV/heat triggering[7] and laser triggering methods. For the UV/heat method, weight change measurements began after 120 °C heat was applied to composites pre-exposed to 365 nm UV for 30 min[7]. In contrast, for the laser-triggering method, weight change measurements began upon applying a pulsed laser (laser power = 0.50 W) from a light source located 5 meters away, without any prior UV exposure. The decomposition rates of the Ecoflex 00-30 and Sylgard-184 composites under laser triggering were approximately 5.3 and 3.5 times faster, respectively, than those under heat treatment at 120 °C following UV exposure. The slower decomposition rates with the UV/heat method can be attributed to non-uniform heat transfer, as a heat gun or hot plate heats only the composite surface during the heating process[7]. In contrast, the laser-triggering method enables more uniform heating, as the laser penetrates the interior of the composite to stimulate Fe_3O_4 NPs throughout its volume, with the additional heat transfer provided by the high thermal conductivity of the photothermal filler. This internal stimulation enables faster, more efficient decomposition than the UV/heat method.

Mechanical behaviors of DPI-HFP/Fe_3O_4 NPs/Ecoflex composite

Figure 4 illustrates the mechanical behavior of DPI-HFP/Fe_3O_4 NPs/Ecoflex composite. Figure 4A shows that the composite sheet (30 mm × 30 mm × 3 mm) exhibited no damage and returned to its original state while maintaining elastic properties after undergoing physical distortion, including uniaxial and biaxial stretching, twisting, and poking. Supplementary Figure 8A presents the uniaxial tensile test results of the DPI-HFP/Fe_3O_4 NPs/Ecoflex composite compared to neat Ecoflex. The composite exhibited a ~ 15.3% increase in modulus, while its ultimate tensile strength (UTS) and elongation at break decreased by ~ 37.7% and ~ 34.0%, respectively, compared to the Ecoflex matrix [Figure 4B]. At low strain levels, the interaction between the rigid fillers and the polymer matrix remains intact, increasing modulus. However, as the material nears rupture, DPI-HFP particles and Fe_3O_4 NPs create voids within the composite, leading to stress concentrations that reduce UTS and elongation[7,41-43].

Supplementary Figure 8B shows the loading-unloading curves for the DPI-HFP/Fe_3O_4 NPs/Ecoflex composite and Ecoflex over the strain range of 100%-400%. The hysteresis loss ratios of the composite were ~ 20.2%, 17.5%, 18.3%, and 21.7%, while Ecoflex exhibited values of ~ 1.6%, 6.0%, 10.1%, and 18.3% at strains of 100%, 200%, 300%, and 400%, respectively [Figure 4C]. The higher hysteresis loss in the composite is attributed to increased frictional forces between the fillers and the polymer chains, which interrupt recovery[44-46]. Although filler incorporation slightly reduces the mechanical performance compared to Ecoflex alone, the composite still maintains excellent elongation and resilience. In a cyclic loading-unloading test performed up to 200% strain, the 100th cycle exhibits a cyclic stress softening ratio of ~ 17.97% [Supplementary Figure 8C and D]. Here, the cyclic stress softening ratio is defined as the relative decrease in

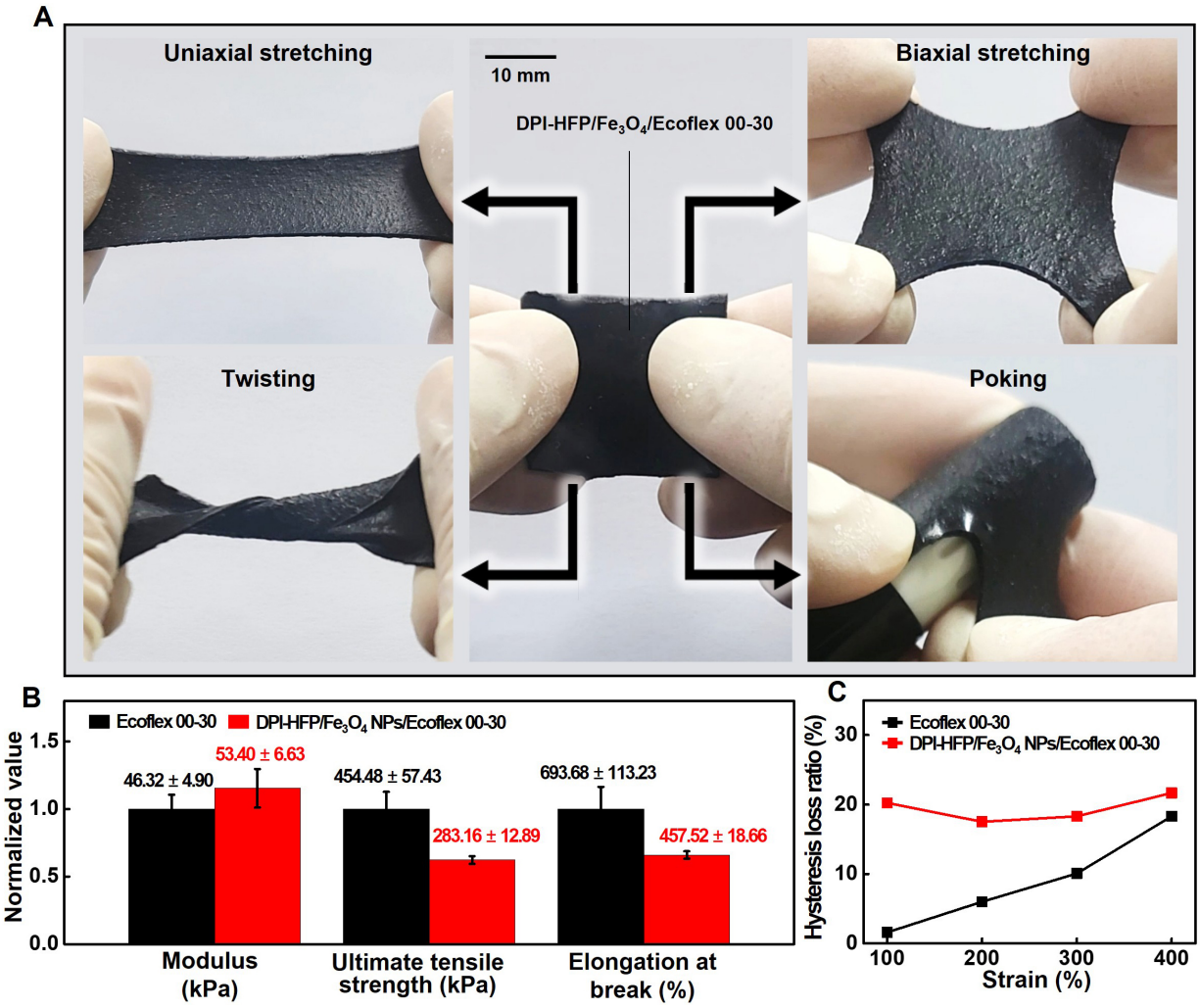

Figure 4. Mechanical properties of DPI-HFP/Fe_3O_4 NPs/Ecoflex 00-30 composite. (A) Photographic images of DPI-HFP/Fe_3O_4 NPs (1.00 wt.%)/Ecoflex 00-30 composite sheet (middle), which is uniaxially stretched (top left), biaxially stretched (top right), twisted (bottom left), and poked (bottom right); (B) Relative mechanical properties of neat Ecoflex 00-30 (black) and DPI-HFP/ Fe_3O_4 NPs/Ecoflex 00-30 composite (red); (C) Variation in hysteresis loss ratio of neat Ecoflex 00-30 (black) and DPI-HFP/ Fe_3O_4 NPs/Ecoflex 00-30 composite (red) with respect to strain range (100-400%). (B) Data are presented as mean ± SD of n = 3 independent measurements. NP: Nanoparticle; DPI-HFP: diphenyliodonium hexafluorophosphate; SD: standard deviation.

the area under the loading stress-strain curve from the first cycle to the 100th cycle. In addition, the variation in mechanical properties, including elastic modulus, ultimate tensile strength, and elongation at break, remained within 13.7% after storage under ambient conditions for 14 days [Supplementary Figure 8E and F]. These mechanical properties make it well-suited for applications in degradable stretchable electronics and soft actuators, where both deformability and structural integrity are required[7,8,47,48].

Application to laser-triggered transient soft and stretchable electronics

The DPI-HFP/Fe_3O_4 NPs/Ecoflex composite exhibits longer triggering distance, superior mechanical properties, and reasonable stability, compared to previously reported triggerable transient materials [Supplementary Table 1], making it a promising platform for applications in soft electronics and soft robotics. The integration of this composite substrate, which exhibits excellent elongation and resilience, with nanoscale inorganic electrodes in a serpentine geometry enables the realization of laser-triggered transient soft and stretchable electronics. Figure 5 shows the characteristics and decomposition behaviors of soft and stretchable electronics assembled on DPI-HFP/Fe_3O_4 NPs (1.00 wt.%)/Ecoflex 00-30 substrates.

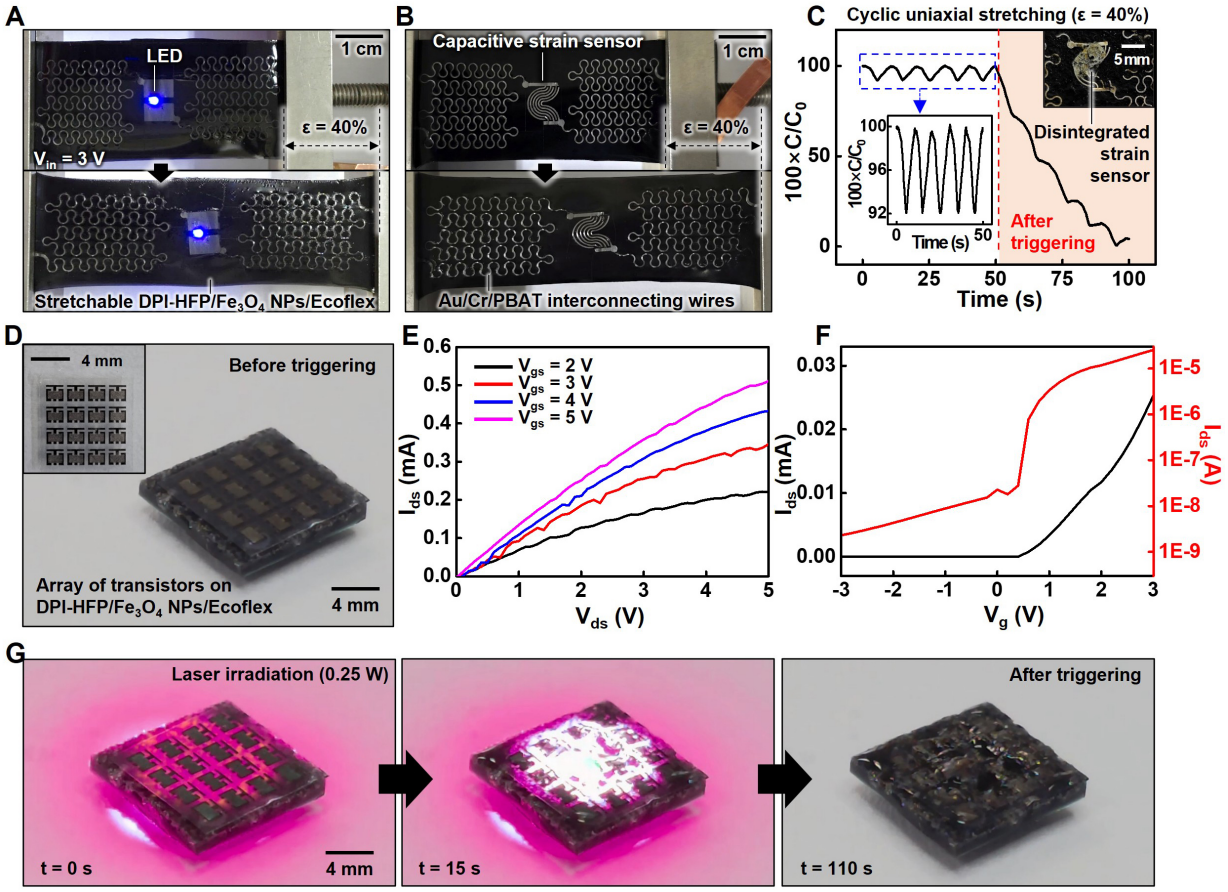

Figure 5. Laser-triggered transient electronics on stretchable DPI-HFP/Fe_3O_4 NPs/Ecoflex 00-30 substrate. Images of (A) a blue LED and (B) an interdigitated capacitive strain sensor connected to serpentine interconnecting wires composed of Au (~ 75 nm)/Cr (~ 15 nm)/PBAT (~ 30 μm), integrated on a stretchable DPI-HFP (10 wt.%)/Fe_3O_4 NPs (1.00 wt.%)/Ecoflex 00-30 substrate (~ 220 μm), before (top) and after (bottom) uniaxial stretching (uniaxial strain = 40 %). In the top view, the interconnecting wires appear light gray due to the Cr layer beneath the transparent PBAT layer, which covers the underlying Au layer directly interfaced with the composite substrate; (C) Capacitance change of the strain sensor before and after laser triggering in the middle of 10 cycles of uniaxial stretching at 40% strain (strain rate = 8% s^{-1}). A 0.25 W laser was irradiated after the fifth cycle; (D) Images showing a 4 × 4 array of n-channel MOSFETs composed of Si NMs (~ 400 nm), SiO_2 gate dielectric (~ 100 nm), Mo electrodes (~ 400 nm), and PBAT top layer (~ 30 μm) integrated on a DPI-HFP/Fe_3O_4 NPs/Ecoflex substrate. The inset shows a top view of the MOSFET array before integration onto the composite substrate; (E) I-V curve and (F) transfer curve of an n-channel MOSFET on the composite substrate; (G) Images showing the MOSFET array during (left and middle) and after (right) the 800 nm laser irradiation (spot size = 8 mm (diameter), pulse width = ~ 100 fs, power = 0.25 W) for 110 s. LED: Light-emitting diode; PBAT: polybutylene adipate terephthalate; NP: nanoparticle; DPI-HFP: diphenyliodonium hexafluorophosphate; MOSFET: metal-oxide-semiconductor field-effect transistor; NM: nanomembrane.

Figure 5A and B show two representative devices: a blue LED and an interdigitated capacitive strain sensor, each connected to Au/Cr/PBAT serpentine interconnecting wires on the stretchable composite substrate. The interconnecting wires, electrode pads for the LED, and the strain sensor were fabricated by laser-patterning a PBAT film (~ 30 μm) sequentially sputter-deposited with Cr (~ 15 nm) and Au (~ 75 nm). Uncured composite resin was then poured over the Au layer to a thickness of ~ 1 mm, followed by curing to form the stretchable composite substrate [Supplementary Figure 9]. The LED, driven at 3 V DC, maintained comparable brightness under 40% uniaxial strain [Figure 5A] and remained operational up to ~ 48% strain owing to serpentine geometry [Supplementary Figure 10].

The strain sensor likewise showed no visible cracking in the inorganic layers at 40% uniaxial strain [Figure 5B]. Its capacitance decreased approximately linearly from 3.25 pF to 2.41 pF over 0%-40% strain due to tensile-induced increases in electrode spacing for the interdigitated layout [Supplementary Figure 11A][7].

Figure 5C plots capacitance during cyclic stretching between 0%-40% strain (one cycle per 10 s), before and after laser triggering. As highlighted in the inset, the sensor produced stable, periodic capacitance waveforms over the initial five cycles. At 50 s, stand-off laser irradiation (800 nm, ~ 100 fs pulses, 0.25 W, 5 m) initiated decomposition; by 100 s the device had collapsed (inset photograph), retaining only ~ 4.3% of the initial capacitance. Beyond capacitors, a resistor malfunctioned after ~ 1 min of laser exposure [Supplementary Figure 12 and Supplementary Video 6], and a 4 × 3 temperature-sensor array (resistive elements on an ultrathin composite) exhibited sufficient stretchability and conformal contact [Supplementary Figures 13 and 14]. Detailed designs, characterizations, and disintegration behaviors of the resistor and temperature array are provided in the Supplementary Text.

Laser-triggered destruction was also demonstrated in silicon-based devices, leading to the structural collapse of the composite substrate and the formation of heat and gaseous byproducts from thermochemical reactions. The test vehicle was an NMOS array fabricated on a PBAT film (~ 30 μm) laminated to the composite (~ 1 mm) by transfer printing phosphorus-doped Si nanomembranes (~ 400 nm), PECVD deposition of a SiO_2 gate dielectric (~ 100 nm), and sputtering of Mo electrodes (~ 400 nm) [Figure 5D]. A representative device exhibited a linear-regime mobility of ~ 332 $cm^2 V^{-1} s^{-1}$ and an on/off ratio of ~ 10^4 [Figure 5E and F].

Upon triggering the 0.25 W laser, inorganic components and the PBAT support began to fail within ~ 15 s; complete collapse occurred by 110 s, with the formation of liquid residues at the composite surface [Figure 5G and Supplementary Video 7]. These observations indicate that device destruction is governed primarily by (i) phase change and mechanical collapse of the silicone composite driven by Si-O bond scission and (ii) thermal softening/melting of the thermoplastic PBAT. Increasing fluoride-ion generation within the substrate is expected to enhance device destruction for security applications, as fluoride species can chemically attack common dielectrics (SiO_2, Si_3N_4) and metals (e.g., Al, Mg, Cu)[7,49-52].

Application for on-demand, remotely triggerable soft robots

The high elasticity of our laser-triggered transient composite enables its application to on-demand, remotely triggerable soft robots. These can be either entirely transient soft robots that fully decompose or shape-shifting soft robots that alter their form and function by selectively decomposing specific components. The ability to trigger these remotely at desired times enhances the potential applications of transient soft robots, such as secure exploration robots that quickly decompose to hide sensitive information or waste-free robots that dissolve and vanish after their operational lifetime[7,8,18,48,53-55]. Additionally, in shape-shifting robots, this feature allows their body frames to be rapidly transformed to meet environmental demands, offering advantages in natural exploration and terrain adaptation[14-16]. As an example of such applications, we demonstrated a transformable soft actuator whose motion can be modulated via remote control, utilizing a laser-triggered transient composite as the strain limiter [Figure 6].

The strain limiters, made of the DPI-HFP/Fe_3O_4 NPs/Sylgard-184 composite, are positioned at the top-right and bottom-left corners of a zigzag-shaped actuator constructed from Ecoflex 00-30 [Figure 6A, top left]. When pneumatic pressure is applied to the air channel, the actuator exhibits an S-type motion due to the modulus difference between the soft Ecoflex 00-30 bladder and the relatively stiff Sylgard-184 strain limiters. Laser decomposition of the top-right strain limiter (λ = 800 nm, pulse width ~ 100 fs, 0.5 W) transforms the actuator into a J-type motion [Figure 6A, top right]. Triggering the bottom-left strain limiter further alters the motion from J-type to I-type [Figure 6A, bottom right]. Changing the sequence of strain limiter activation alters the motion transformation path. For instance, decomposing the bottom-right strain limiter results in a C-type motion [Figure 6A, bottom left], and subsequently triggering the top-right strain limiter transitions the motion from C-type to I-type [Figure 6A, bottom right]. Instead of assembling, disassembling,

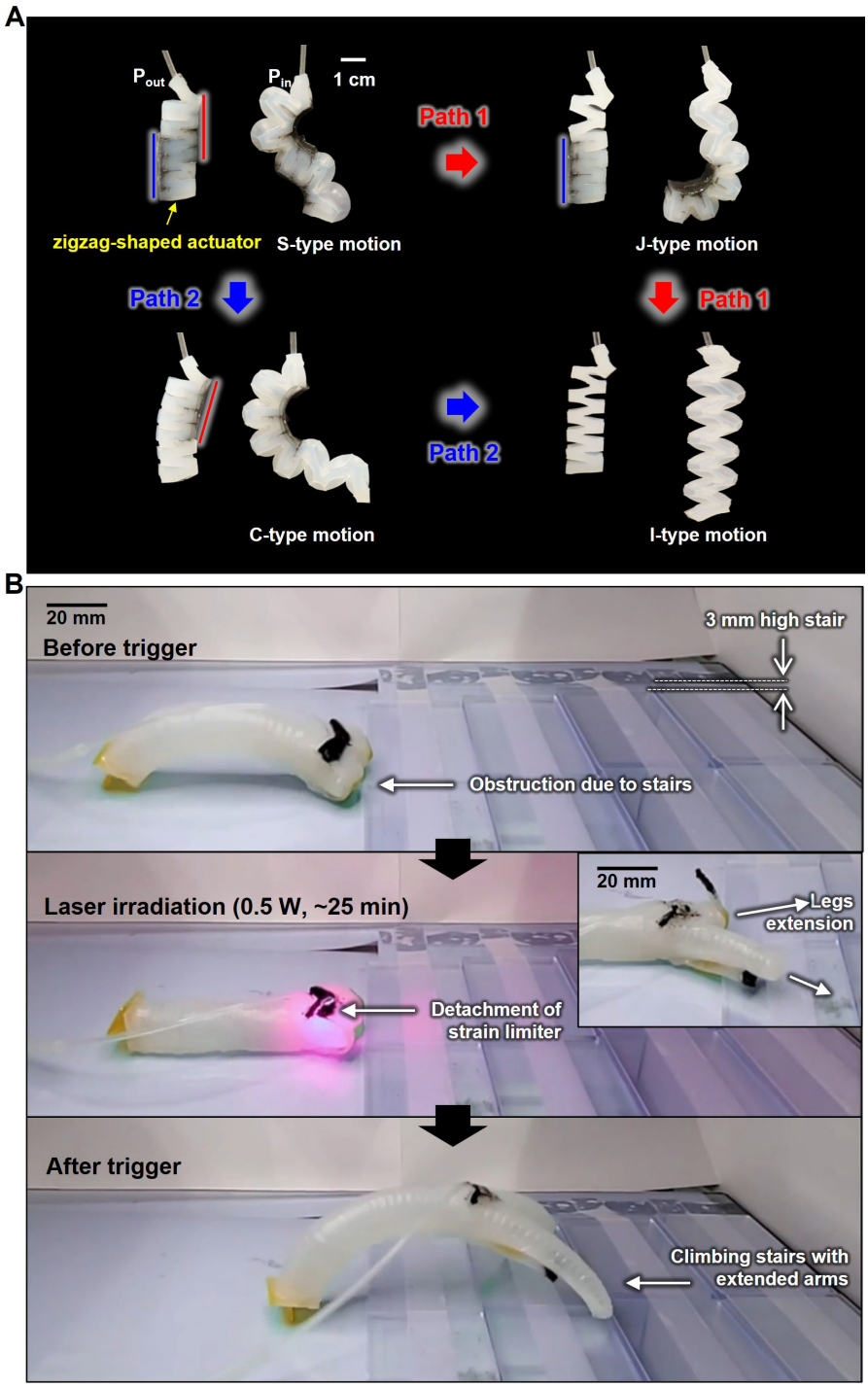

Figure 6. On-demand remote transformation of soft robots. (A) Photographic images of zigzag shape actuation before triggering, J-type actuation after top-right strain limiter triggering, C-type actuation after bottom-left strain limiter triggering, and I-type actuation after full triggering (spot size = 8 mm (diameter), laser power = 0.5 W, λ = 800 nm, pulse width = ~ 100 fs). (B) Image of the legless soft crawler blocked by a 3 mm high step (top). Image showing the midpoint of laser triggering (middle) and leg extension (middle, inset). Image depicting the successful stair climbing of the transformed 2-leg soft crawler (bottom).

and reconfiguring individual modules[56,57], this approach of partially decomposing and reconfiguring the strain limiter pattern within a single-chamber soft actuator to generate new trajectories is a promising method for improving efficiency and miniaturization. Notably, throughout the laser-triggering process, the neat Ecoflex adjacent to the strain limiters experienced minimal damage, with a ~ 13.4% decrease in elongation and a ~ 17.2% reduction in UTS [Supplementary Figure 15].

Inducing shape-shifting of the robot via remote triggering is not limited to simply altering the trajectory of a single chamber; it can also be applied by adding functional frames. We demonstrated this concept using a leg-expanding crawler robot. Supplementary Figure 16 illustrates the components and crawling mechanisms of a legless soft crawler and a 2-leg soft crawler transformed via remote laser triggering. The legless soft crawler comprises a hollow, cylindrical bending body with inverted bending legs rolled inward [Supplementary Figure 16A, left]. Strain limiters sealed the openings to prevent leg extension during inflation. These strain limiters were fabricated from Ecoflex 00-30 sheets and adhered using triggerable adhesive made from DPI-HFP/Fe_3O_4 NPs (1.00 wt.%)/Ecoflex 00-30. The bending body itself was constructed by rolling an Ecoflex 00-30 sheet embedded with evenly spaced fibers and sealing it with high-modulus Dragon Skin [Supplementary Figure 16A, right]. To reduce ground friction, PI tape was attached to the front strain limiter, while Dragon Skin 20 supports the rear [Supplementary Figure 16A, right, inset]. Upon remote laser triggering, the adhesive dissolves, allowing the strain limiters to partially detach and enabling the legs to extend during inflation [Supplementary Figure 16B, left]. The bending legs were constructed similarly to the bending body, using Ecoflex 00-30 sheets, fibers, and Dragon Skin 20 [Supplementary Figure 16B, right]. Supplementary Figure 16C and D and Supplementary Videos 8 and 9 show sequential photographic frames and movies of the crawling motion of the legless soft crawler before triggering and the 2-leg soft crawler after triggering, respectively. Both crawlers achieved a forward motion of approximately 20 mm per spike.

The extended legs of the 2-leg crawler demonstrated the potential to overcome obstacles such as stairs [Figure 6B]. A stair model made of 3 mm-high glass steps was prepared [Figure 6B, top] to evaluate the terrain-traversal performance of the 2-leg soft crawler. The initial legless crawler was unable to ascend the first step. After decomposing the triggerable adhesive with a laser (λ = 800 nm, pulse width ~ 100 fs, 0.5 W) [Figure 6B, middle], the inflation of the crawler extended the previously rolled-in legs [Figure 6B, middle, inset]. The slightly elevated tips of the extended legs enabled the crawler to climb the steps during crawling [Figure 6B, bottom]. Additional photographs and movies of this demonstration are provided in Supplementary Figure 17 and Supplementary Video 10. This transformable soft robot, equipped with extendable modules, has significant potential for applications such as exploring uncharted terrain or conducting search operations, especially with further diversification of its modules. Nevertheless, the irreversible nature of this transformation may impose limitations on systems that require repeated structural reconfiguration. Future approaches, such as partial or graded decomposition, modular design, and multi-stimulus triggering systems, could further enhance reusability and functional versatility.

CONCLUSIONS

This study presents an elastomeric composite for rapid, remotely triggered decomposition, combining a silicone matrix with photothermal Fe_3O_4 NPs and the thermally activated fluoride generator DPI-HFP. Femtosecond laser activation induces fluoride release, catalyzing Si-O bond cleavage while consuming only ~ 5.4% of the energy required for direct laser ablation. The decomposition rate is tunable through filler content and laser power, and the composite retains high elasticity for use in transient soft electronics and transformable soft actuators. Laser-based triggering enables stand-off control with high spatial precision, eliminating the need for bulky actuation hardware and supporting operation in inaccessible or constrained environments. Future research will focus on simplifying laser systems (e.g., compact, low-power light sources for practical deployment) to facilitate broader adoption, and incorporating fluoride-capture approaches (e.g., scavenging additives or encapsulation strategies) to enhance safety and sustainability.

DECLARATIONS

Authors' contributions

Conceptualization: Kim, K. S.; Oh, M. H.; Kim, S. Y.; Kang, S. K.

Methodology: Kim, K. S.; Oh, M. H.; Han, J.; Kim, Y. N.; Bae, J. Y.; Kim. Y. W.; Shin, Y. J.; Lee, J. H.; Kim, S. W.; Wyszkowska, E.

Investigation: Kim, K. S.; Oh, M. H.; Han, J.; Kim, Y. N.; Kim. Y. W.
Writing: Kim, K. S.; Oh, M. H.; Kim, Y. N.; Bae, J. Y.; Kang, S. K.
Supervision: Kim, S. Y.; Kang, S.-K.

Availability of data and materials

All the data generated and/or analyzed during the current study are available in this published article and its Supplementary Materials. The datasets used and/or analyzed during the current study are available from the corresponding author on reasonable request.

AI and AI-assisted tools statement

During the preparation of this manuscript, the AI tools, including ChatGPT (GPT-5.3, released 2026-03-01) and Grammarly (14.1287.0, released 2026-04-27), were used solely for language editing. The tool did not influence the study design, data collection, analysis, interpretation, or the scientific content of the work. All authors take full responsibility for the accuracy, integrity, and final content of the manuscript.

Financial support and sponsorship

This work is supported by the National R&D Program through the National Research Foundation of Korea, funded by the Ministry of Science and ICT (Grant No. RS-2025-02305569), and by the Korea Institute of Energy Technology Evaluation and Planning (KETEP) and the Ministry of Trade, Industry & Energy (MOTIE) of the Republic of Korea (Grant No. RS-2023-00303582).

Conflicts of interest

Kang, S. K. is a Guest Editor of the Special Issue entitled "Transient and Biodegradable Soft Electronics and Robots for Sustainable and Biomedical Applications" in *Soft Science*. He is not involved in any steps of editorial processing, notably including reviewers' selection, manuscript handling and decision making. Oh, M. H. is affiliated with Samsung Electronics Co. Ltd. The other authors declare that there are no conflicts of interest.

Ethical approval and consent to participate

Not applicable.

Consent for publication

Not applicable.

Supplementary Materials

Supplementary Materials

REFERENCES

1. Walther, A. Viewpoint: from responsive to adaptive and interactive materials and materials systems: a roadmap. *Adv. Mater.* **2019**, *32*, 1905111. DOI PubMed PMC
2. Kang, S. H. Dynamically adaptive materials. *MRS. Bulletin.* **2024**, *49*, 1121-6. DOI
3. Liu, Y.; Han, J.; Yan, W.; et al. Degradable epoxy resins derived from α-terpineol: synthesis, characterization and application in thermally conductive adhesives. *Polymer* **2025**, *336*, 128955. DOI
4. Miao, W.; Laamari, L. S.; Yu, J.; et al. A shape-adaptive, performance-programmable, self-healable and on-demand destructible robotic skin via self-strengthening dynamic silicone. *Adv. Sci.* **2025**, *13*, e08823. DOI
5. Cho, W.; Kang, D. J.; Hahm, M. J.; et al. Multi-functional locomotion of collectively assembled shape-reconfigurable electronics. *Nano. Energy.* **2023**, *118*, 108953. DOI
6. Istif, E.; Ali, M.; Ozuaciksoz, E. Y.; Morova, Y.; Beker, L. Near-infrared triggered degradation for transient electronics. *ACS. Omega.* **2024**, *9*, 2528-35. DOI PubMed PMC
7. Oh, M.; Kim, Y.; Lee, S.; et al. Lifetime-configurable soft robots via photodegradable silicone elastomer composites. *Sci. Adv.* **2023**, *9*, eadh9962. DOI PubMed PMC

8. Kim, Y. N.; Jeon, W.; Oh, M. H.; Seo, H. J.; Kwon, M. S.; Kang, S. K. UV-triggered cascading degradation of silicone elastomer via self-fluoride amplification. *Adv. Sci.* **2025**, *12*, e02056. DOI
9. Byun, S.; Sim, J. Y.; Zhou, Z.; et al. Mechanically transformative electronics, sensors, and implantable devices. *Sci. Adv.* **2019**, *5*, eaay0418. DOI PubMed PMC
10. Lee, S.; Lee, G.; Kang, I.; et al. Phase-change metal ink with pH-controlled chemical sintering for versatile and scalable fabrication of variable stiffness electronics. *Sci. Adv.* **2025**, *11*, eadv4921. DOI PubMed PMC
11. Aksoy, B.; Shea, H. Multistable shape programming of variable-stiffness electromagnetic devices. *Sci. Adv.* **2022**, *8*, eabk0543. DOI PubMed PMC
12. Gao, Y.; Zhang, Y.; Wang, X.; et al. Moisture-triggered physically transient electronics. *Sci. Adv.* **2017**, *3*, e1701222. DOI PubMed PMC
13. Lee, D.; Rubab, N.; Hyun, I.; et al. Ultrasound-mediated triboelectric nanogenerator for powering on-demand transient electronics. *Sci. Adv.* **2022**, *8*, eabl8423. DOI PubMed PMC
14. Hinchet, R.; Shea, H. High force density textile electrostatic clutch. *Adv. Mater. Technologies.* **2019**, *5*, 1900895. DOI
15. Campbell, G. M.; Roosa, R. D.; Turner, K.; Pikul, J.; Yim, M. Control of silicone-sheathed electrostatic clutches for soft pneumatic actuator position control. In *2024 IEEE 7th International Conference on Soft Robotics (RoboSoft)*, San Diego, CA, USA, April 14-17, 2024; IEEE, 2024, pp 299-304. DOI
16. Yang, B.; Baines, R.; Shah, D.; et al. Reprogrammable soft actuation and shape-shifting via tensile jamming. *Sci. Adv.* **2021**, *7*, eabh2073. DOI PubMed PMC
17. Wang, H.; Chen, S.; Zhu, X.; et al. Phase transition science and engineering of gallium-based liquid metal. *Matter* **2022**, *5*, 2054-85. DOI
18. Mariani, S.; Cecchini, L.; Pugno, N. M.; Mazzolai, B. An autonomous biodegradable hygroscopic seed-inspired soft robot for visual humidity sensing. *Mater. Des.* **2023**, *235*, 112408. DOI
19. Yang, H.; Xu, K.; Xu, C.; et al. Femtosecond laser fabricated elastomeric superhydrophobic surface with stretching-enhanced water repellency. *Nanoscale. Res. Lett.* **2019**, *14*, 333. DOI PubMed PMC
20. Sadat, M. E.; Kaveh Baghbador, M.; Dunn, A. W.; et al. Photoluminescence and photothermal effect of Fe3O4 nanoparticles for medical imaging and therapy. *Appl. Phys. Lett.* **2014**, *105*, 091903. DOI
21. Johnson, R. J. G.; Haas, K. M.; Lear, B. J. Fe_3O_4 nanoparticles as robust photothermal agents for driving high barrier reactions under ambient conditions. *Chem. Commun.* **2015**, *51*, 417-20. DOI
22. Wang, X.; Dai, L.; Jiao, N.; Tung, S.; Liu, L. Superhydrophobic photothermal graphene composites and their functional applications in microrobots swimming at the air/water interface. *Chem. Eng. J.* **2021**, *422*, 129394. DOI
23. Gong, J.; Ding, Q.; Shi, Y.; et al. NIR-responsive gold nanomaterials in photothermal antibacterial therapy: from morphological design to multifunctional platforms. *Coord. Chem. Rev.* **2025**, *526*, 216348. DOI
24. Haas, K. M.; Lear, B. J. Degradation of polypropylene carbonate through plasmonic heating. *Nanoscale* **2013**, *5*, 5247. DOI
25. Liu, X.; Zhao, Z.; Xie, X.; et al. Ultrahigh thermal conductivity and photothermal conversion in interface-optimized bacterial cellulose/boron nitride nanosheets/MXene composites. *J. Mater. Sci. Technol.* **2026**, *248*, 87-98. DOI
26. Liu, X.; Lin, F.; Leng, G.; et al. A high thermal conductive composite phase change film for flexible solar/electro-thermal energy conversion. *J. Energy. Storage.* **2023**, *73*, 108959. DOI
27. Huang, L.; Ning, J.; Yang, Y.; et al. Thermal-conductive, dynamic cross-linked solid-solid phase change composites toward sustainable energy utilization. *Ind. Eng. Chem. Res.* **2022**, *61*, 6448-57. DOI
28. Li, J.; Zhang, W.; Ji, W.; et al. Near infrared photothermal conversion materials: mechanism, preparation, and photothermal cancer therapy applications. *J. Mater. Chem. B.* **2021**, *9*, 7909-26. DOI
29. Bellier, M.; Ali, M. E. A.; Abo El Fadl, M. M.; Perreault, F. Photothermal carbon black nanoparticle coating increases scaling resistance in solar membrane distillation. *ACS. EST. Water.* **2024**, *4*, 5925-32. DOI
30. Lam, K. Y.; Lee, C. S.; Tan, R. Y. H. NIR-induced photothermal-responsive shape memory polyurethane for versatile smart material applications. *RSC. Adv.* **2024**, *14*, 24265-86. DOI PubMed PMC
31. Bibinger, J.; Eibl, S.; Gudladt, H.; Schartel, B.; Höfer, P. Pushing the limits of thermal resistance in nanocomposites: a comparative study of carbon black and nanotube modifications. *Nanomaterials* **2025**, *15*, 546. DOI PubMed PMC
32. Rabbi, K. M.; Saha, S.; Mojumder, S.; Rahman, M.; Saidur, R.; Ibrahim, T. A. Numerical investigation of pure mixed convection in a ferrofluid-filled lid-driven cavity for different heater configurations. *Alex. Eng. J.* **2016**, *55*, 127-39. DOI
33. Azimi-juybari, H.; Mohagheghi, M. B. The significance of the synthesis method for graphite-like carbon: effects of acidifying agents on properties and carbon monoxide sensitivity. *J. Mater. Sci:. Mater. Electron.* **2025**, *36*, 319. DOI
34. Song, J.; Tian, K.; Ma, L.; Li, W.; Yao, S. The effect of carbon black morphology to the thermal conductivity of natural rubber composites. *Int. J. Heat. Mass. Transfer.* **2019**, *137*, 184-91. DOI
35. Rajkumar, N.; Umamahaeswari, D.; Ramachandran, K. Photoacoustics and magnetic studies of Fe_3O_4 nanoparticles. *Int. J. Nanosci.* **2011**, *09*, 243-50. DOI

36. Sailor, M. J. Chemical reactivity and surface chemistry of porous silicon. In *Handbook of Porous Silicon*; Canham, L., Eds.; Springer International Publishing, 2014; pp 355-80. DOI
37. Isohashi, A.; Bui, P. V.; Toh, D.; et al. Chemical etching of silicon carbide in pure water by using platinum catalyst. *Appl. Phys. Lett.* **2017**, *110*, 201601. DOI PubMed PMC
38. Son, C. E.; Choi, S. S. Analytical techniques for measurement of crosslink densities of rubber vulcanizates. *Elastom. Compos.* **2019**, *54*, 209-19. DOI
39. Fu, S.; Man, Y.; Jia, F. Photothermal effect of superparamagnetic Fe_3O_4 nanoparticles irradiated by near-infrared laser. *J. Nanomater.* **2020**, *2020*, 1-8. DOI
40. Weber, R.; Graf, T.; Berger, P.; et al. Heat accumulation during pulsed laser materials processing. *Opt. Express.* **2014**, *22*, 11312. DOI
41. Salmah, H.; Koay, S.; Hakimah, O. Surface modification of coconut shell powder filled polylactic acid biocomposites. *J. Thermoplast. Compos. Mater.* **2012**, *26*, 809-19. DOI
42. Yu, Y.; Kong, L.; Li, L.; Li, N.; Yan, P. Antitumor activity of doxorubicin-loaded carbon nanotubes incorporated poly(lactic-co-glycolic acid) electrospun composite nanofibers. *Nanoscale. Res. Lett.* **2015**, *10*, 343. DOI PubMed PMC
43. Fu, S.; Feng, X.; Lauke, B.; Mai, Y. Effects of particle size, particle/matrix interface adhesion and particle loading on mechanical properties of particulate-polymer composites. *Compos. Part. B-Eng.* **2008**, *39*, 933-61. DOI
44. Chattopadhyay, P. K.; Chattopadhyay, S.; Das, N. C.; Bandyopadhyay, P. P. Impact of carbon black substitution with nanoclay on microstructure and tribological properties of ternary elastomeric composites. *Mater. Des.* **2011**, *32*, 4696-704. DOI
45. Lozano-Pérez, C.; Cauich-Rodríguez, J.; Avilés, F. Influence of rigid segment and carbon nanotube concentration on the cyclic piezoresistive and hysteretic behavior of multiwall carbon nanotube/segmented polyurethane composites. *Compos. Sci. Technol.* **2016**, *128*, 25-32. DOI
46. Lorenz, H., Meier, J., Klüppel, M. Micromechanics of internal friction of filler reinforced elastomers. In *Elastomere Friction*; Besdo, D., Heimann, B., Klüppel, M., Kröger, M., Wriggers, P., Nackenhorst, U., Eds.; Lecture Notes in Applied and Computational Mechanics, Vol. 51; Springer Berlin Heidelberg, 2010; pp 27-52. DOI
47. Choi, Y. S.; Hsueh, Y.; Koo, J.; et al. Stretchable, dynamic covalent polymers for soft, long-lived bioresorbable electronic stimulators designed to facilitate neuromuscular regeneration. *Nat. Commun.* **2020**, *11*, 5990. DOI PubMed PMC
48. Han, W. B.; Ko, G.; Lee, K.; et al. Ultra-stretchable and biodegradable elastomers for soft, transient electronics. *Nat. Commun.* **2023**, *14*, 2263. DOI PubMed PMC
49. Subramanian, M. A.; Manzer, L. E. A "greener" synthetic route for fluoroaromatics via copper (II) fluoride. *Science* **2002**, *297*, 1665. DOI
50. Ritala, H.; Kiihamäki, J.; Heikkilä, M. Studies on aluminium corrosion during and after HF vapour treatment. *Microelectron. Eng.* **2010**, *87*, 501-4. DOI
51. Kwon, D.; Pham, H. V.; Song, P.; Moon, S. Corrosion behavior of the AZ31 Mg alloy in neutral aqueous solutions containing various anions. *Metals* **2023**, *13*, 962. DOI
52. Son, C.; Lim, S. Editors' choice - control of Si_3N_4 etching kinetics and selectivity to SiO_2 by the additives in superheated water. *ECS. J. Solid. State. Sci. Technol.* **2019**, *8*, N85-91. DOI
53. Hartmann, F.; Baumgartner, M.; Kaltenbrunner, M. Becoming sustainable, the new frontier in soft robotics. *Adv. Mater.* **2020**, *33*, 2004413. DOI
54. Wiesemüller, F.; Meyer, S.; Hu, Y.; et al. Biopolymer cryogels for transient ecology-drones. *Adv. Intell. Syst.* **2023**, *5*, 2300037. DOI
55. Cikalleshi, K.; Nexha, A.; Kister, T.; et al. A printed luminescent flier inspired by plant seeds for eco-friendly physical sensing. *Sci. Adv.* **2023**, *9*, eadi8492. DOI PubMed PMC
56. Legrand, J.; Terryn, S.; Roels, E.; Vanderborght, B. Reconfigurable, multi-material, voxel-based soft robots. *IEEE. Robot. Autom. Lett.* **2023**, *8*, 1255-62. DOI
57. Atia, M. G. B.; Mohammad, A.; Gameros, A.; Axinte, D.; Wright, I. Reconfigurable soft robots by building blocks. *Adv. Sci.* **2022**, *9*, 2203217. DOI